

*Under consideration for publication in J. Fluid Mech.*

1

# The crossflow instability of the boundary layer on a rotating cone

S. J. Garrett <sup>1</sup>, Z. Hussain <sup>2</sup> AND S. O. Stephen <sup>2</sup>

<sup>1</sup>Department of Mathematics, University of Leicester, University Road,  
Leicester LE1 7RH, UK

<sup>2</sup>School of Mathematics, University of Birmingham, Birmingham B15 2TT, UK

(Received 19 November 2007)

Experimental studies have shown that the boundary-layer flow over a rotating cone is susceptible to crossflow and centrifugal instability modes of spiral nature, depending on the cone sharpness. For half-angles ( $\psi$ ) ranging from propeller nose cones to rotating disks ( $\psi \geq 40^\circ$ ), the instability triggers co-rotating vortices; whereas for sharp spinning missiles ( $\psi < 40^\circ$ ), counter-rotating vortices are observed. In this paper we provide a mathematical description of the onset of co-rotating vortices for a family of cones rotating in quiescent fluid, with a view towards explaining the effect of  $\psi$  on the underlying transition of dominant instability. We investigate the stability to inviscid crossflow modes (type I), as well as modes which arise from a viscous-Coriolis force balance (type II), using numerical and asymptotic methods. The influence of  $\psi$  on the number and orientation of the spiral vortices is examined, with comparisons drawn between our two distinct methods, as well as with previous experimental studies.

Our results indicate that increasing  $\psi$  has a stabilizing effect on both the type I and type II modes. Favourable agreement is obtained between the numerical and asymptotic methods presented here and existing experimental results for  $\psi > 40^\circ$ . Below this half-angle we suggest that an alternative instability mechanism is at work which is not amenable to investigation using the formulation presented here.

---

## 1. Introduction

There has been considerable interest in the exact mechanisms governing the stability of three-dimensional boundary-layer flows in recent decades, with application to the modern-day design of laminar aerofoils. A great deal of emphasis has been placed on understanding the instability mechanisms that lead to the breakdown of the boundary layer (see the comprehensive reviews by Reed & Saric (1989), Reshotko (1994) and Saric *et al.* (2003) and papers referenced therein). In contrast to the two-dimensional case, the three-dimensional boundary layer exhibits both streamwise and cross-stream flow components. This is reflected in the fact that stream-wise Tollmien-Schlichting waves, crossflow instabilities and centrifugal instabilities all play a part in the transition of such flows; the interplay of these three fundamental mechanisms being dictated by the particular geometry under question. In this study we investigate the rotating-cone boundary layer in quiescent fluid.

The influential study of Gregory *et al.* (1955) contains the first observation of the stationary crossflow vortex pattern on a rotating disk, which is closely related to the rotating cone. Malik (1986) presents numerical solutions for the curves of neutral-stability. Using

a parallel-flow approximation as well as including streamline curvature and Coriolis effects, he shows that there exist two distinct neutral branches which are termed type I and II respectively. † Malik's results were later verified by the linear asymptotic analysis of Hall (1986), who recovered Stuart's type I solution along with the type II branch.

The first experimental investigations of boundary-layer flow over rotating cones in quiescent fluid were carried out by Kreith *et al.* (1962), Tien & Campbell (1963) and Kappesser *et al.* (1973). The scope was restricted to measuring Reynolds numbers at the onset of transition, whereas later Kobayashi & Izumi (1983), using hot-wire techniques, refined the transition structure within the boundary layer leading to the observation of spiral vortices, which are shed under the action of strong distorting forces from the mean-flow field. Interestingly, the vortices were found to be stationary relative to the cone, wrapping round its surface and remaining fixed for all rotation rates. Kobayashi and co-workers have shown that  $\psi$  has a key influence on the nature of vortex rotation. For example, on slender cones with  $\psi$  as low as  $15^\circ$ , Kobayashi & Izumi (1983) show the existence of pairs of counter-rotating Görtler vortices. These arise from a dynamic instability induced by the centrifugal force of the flow field. However, as  $\psi$  is increased beyond, say,  $30^\circ$ , they observe co-rotating spiral vortices. Indeed, Kobayashi (1994) states that co- and counter-rotating vortices coexist for  $\psi = 30^\circ$  – the apparent transitional value for the change of underlying instability. Furthermore, in figure 1c of Kohama (2000), we see an experimental image of circular rings for  $\psi = 30^\circ$ , which may provide a visualisation of the physical transition between the two vortex types. As the cone half-angle tends to  $90^\circ$ , Kobayashi & Izumi's measurements of the spiral angle (the angle between the normal to the vortices and the cone meridian) are shown to approach those observed for a rotating disk. Hence, the stationary spiral crossflow vortices first observed by Gregory *et al.* (1955) on the rotating disk are in fact present for larger values of  $\psi$  on the rotating cone. In addition, Garrett (2002) computes the Reynolds numbers at the onset of convective and absolute instability for the rotating cone and finds close agreement with those experimentally observed at the appearance of spiral vortices and transition to turbulence, respectively. An increasing discrepancy is observed for  $\psi < 50^\circ$ , suggesting an apparent change in the physical nature of the instability which provides the route to transition. In a recent study (Garrett & Peake (2007)), the absolute instability results are developed further and the discrepancy for slender cones is discussed in the context of existing experimental results.

Kobayashi & Izumi (1983) also use local-linear stability theory to predict the onset of convective instability and hence the appearance of the spiral vortices. They consider a family of cones with  $\psi = 15^\circ - 90^\circ$  and critical Reynolds numbers for the onset of the vortices, the vortex angle and number of vortices are predicted at each half-angle. The estimated critical Reynolds numbers agree reasonably well with the experimental values given in their paper. However, the experimental measurements conducted by Kreith *et al.* (1962) and Kappesser *et al.* (1973) agree well with each other for low  $\psi$ , but are substantially different to those of Kobayashi & Izumi. Also, Kobayashi & Izumi provide no information on the instability modes that govern the transition of the boundary layer and so the relative importance of different modes at each half-angle remains unknown.

Physically, wide rotating cones (say  $\psi > 40^\circ$ ) may be considered as a first approximation to modelling, amongst other aerodynamic applications, the central nose rotor of an aeroengine fan. Relatively large half-angles are used to deflect any ensuing turbulent

† In previous studies these respective modes are referred to as either upper/inviscid and lower-branch modes (see Hall (1986) and Malik (1986)), or crossflow and streamline-curvature modes (see Garrett (2002)).

flow away from the turbfan core yet still provide a sufficient amount of airflow into the fan blades. Such physically relevant flows form the basis for our motivation and the aim of the present study is to investigate the effect of  $\psi$  on measurable aerodynamic quantities. We examine the possibility of a critical half-angle, below which the crossflow vortex instability no longer dominates, and also attempt to clarify the points raised in Kobayashi & Izumi's theoretical investigation by using an alternative formulation in the numerical setup. Firstly, we introduce the main scalings used to obtain the steady mean-flow in §2. Next, an asymptotic study at large Reynolds number is presented in §3, where we identify the type I/II modes. Subsequently, the numerical study is presented in §4, where we make a parallel-flow approximation in order to conduct a local spatial stability analysis at points along the cone surface. We demonstrate that the vortices rotate with the surface of the cone and that the wall shear tends to zero along the type II branch, providing a theoretical justification of the assumptions made previously. We proceed to compare the numerical and asymptotic results in §5 both with each other and within the context of existing experimental data. Finally, our conclusions are presented in §6.

## 2. Steady mean flow

This paper presents two analyses performed in different frames of reference and using slightly different scalings. For clarity we present the formulation used within the asymptotic study here, as that is the more mathematically detailed component of the investigation. The modifications to this formulation required for the numerical study are described in §4.1.

Consider a rigid cone of infinite extent with half-angle  $\psi$ , rotating about its axis of symmetry with constant angular velocity  $\Omega^*$  in a fluid of kinematic viscosity  $\nu^*$ , as shown in figure 1. We choose an orthogonal curvilinear coordinate system which rotates with the cone  $(x^*, \theta, z^*)$ , representing streamwise, azimuthal and surface-normal variation, respectively. The local cross-sectional radius of the cone is given by  $r^* = x^* \sin \psi$  (where  $*$  denotes dimensional quantities).

Length quantities are scaled on a characteristic length along the cone surface,  $l^*$ , and the surface-normal coordinate is further scaled on a modified form of the boundary-layer thickness  $(\nu^*/\Omega^* \sin \psi)^{1/2}$ ,

$$x^* = l^* x, \quad z^* = l^* z, \quad z = R^{-1/2} \zeta, \quad (2.1)$$

where  $\zeta$  is the non-dimensional wall-normal coordinate within the boundary layer and  $R$  is the Reynolds number as defined in (2.4). (We shall see that the inclusion of  $\sin \psi^{1/2}$  enables the half-angle to be scaled out of the problem.) The steady velocities are non-dimensionalised using the local surface velocity,  $x^* \Omega^* \sin \psi$ , so the axisymmetric mean flow is

$$\mathbf{u} = \mathbf{u}_b = \Omega^* l^* \sin \psi (x \bar{U}(\zeta), x \bar{V}(\zeta), R^{-1/2} \bar{W}(\zeta)), \quad (2.2)$$

where  $\bar{U}$ ,  $\bar{V}$  and  $\bar{W}$  are the non-dimensional velocities in the  $x^*$ -,  $\theta$ - and  $z^*$ -directions respectively. We scale the steady pressure as

$$p^* = p_b^* = \rho^* \Omega^{*2} l^{*2} \sin^2 \psi R^{-\frac{1}{2}} x \bar{P}(\zeta). \quad (2.3)$$

This particular choice of non-dimensionalisation leads to the Reynolds number

$$R = \frac{\Omega^* l^{*2} \sin \psi}{\nu^*}. \quad (2.4)$$

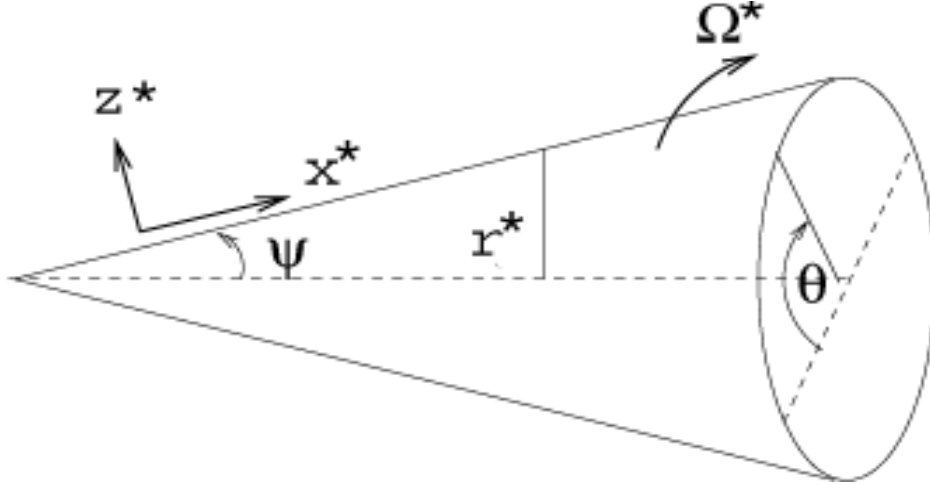


FIGURE 1. Sketch of the coordinate system. The azimuthal axis  $\theta$  rotates with the cone surface.

The relevant continuity and Navier–Stokes equations for the cone geometry are non-dimensionalised using (2.1)–(2.4). Expanding the governing equations in terms of  $R$  and ignoring terms of  $O(R^{-1/2})$ , leads to the familiar von Kármán (1921) equations for boundary-layer flow over a rotating disk, and an additional equation for the pressure:

$$\bar{W}' + 2\bar{U} = 0, \quad (2.5)$$

$$\bar{W}\bar{U}' + \bar{U}^2 - (\bar{V} + 1)^2 = \bar{U}'' , \quad (2.6)$$

$$\bar{W}\bar{V}' + 2\bar{U}(\bar{V} + 1) = \bar{V}'' , \quad (2.7)$$

$$(\bar{V} + 1)^2 \cot \psi = \bar{P}' , \quad (2.8)$$

with boundary conditions

$$\begin{aligned} \bar{U} = 0, \quad \bar{V} = 0, \quad \bar{W} = 0, \quad \text{on } \zeta = 0, \\ \bar{U} \rightarrow 0, \quad \bar{V} \rightarrow -1, \quad \text{as } \zeta \rightarrow \infty. \end{aligned} \quad (2.9)$$

Note that a prime denotes differentiation with respect to  $\zeta$ .

Consequently, we note that this choice of non-dimensionalisation results in  $\psi$  being scaled out of the steady flow equations (2.5)–(2.7) for fluid velocity.

The system of equations (2.5)–(2.7) subject to boundary conditions (2.9) is solved using a fourth-order Runge–Kutta integration method, in conjunction with a two-dimensional Newton–Raphson searching routine. We iterate on the boundary conditions at infinity to produce the well known velocity profiles.

### 3. Asymptotic study

#### 3.1. Linear disturbance equations for the asymptotic analysis

This study uses the formulation introduced in §2. We proceed to linearise the governing equations about the von Kármán steady mean flow profile (2.2) and the basic fluid pressure (2.3) by introducing small perturbation quantities  $\tilde{\mathbf{u}}^*$  and  $\tilde{p}^*$  according to:

$$\mathbf{u}^* = \mathbf{u}_b^* + \tilde{\mathbf{u}}^*, \quad p^* = p_b^* + \tilde{p}^*,$$

where

$$\tilde{\mathbf{u}}^* = \Omega^* l^* \sin \psi (\tilde{u}, \tilde{v}, \tilde{w}), \quad \tilde{p}^* = (\rho^* \Omega^{*2} l^{*2} \sin^2 \psi) \tilde{p}.$$

We non-dimensionalise the governing Navier–Stokes equations and proceed to ignore nonlinear terms. This leads to the linearised perturbation equations:

$$\frac{\partial \tilde{u}}{\partial x} + \frac{\tilde{u} \sin \psi + \tilde{w} \cos \psi}{h} + \frac{1}{h} \frac{\partial \tilde{v}}{\partial \theta} + \frac{\partial \tilde{w}}{\partial z} = 0, \quad (3.1)$$

$$\begin{aligned} & \left( x\bar{U} \frac{\partial}{\partial x} + \frac{x\bar{V}}{h} \frac{\partial}{\partial \theta} + R^{-1/2} \bar{W} \frac{\partial}{\partial z} \right) \tilde{u} + \bar{U} \tilde{u} + x\tilde{w} \frac{\partial \bar{U}}{\partial z} - 2 \left( \frac{x\bar{V} \sin \psi}{h} + 1 \right) \tilde{v} \\ & = -\frac{\partial \tilde{p}}{\partial x} + \frac{1}{R} \left( \nabla^2 \tilde{u} - \frac{(\tilde{u} \sin \psi + \tilde{w} \cos \psi) \sin \psi}{h^2} - \frac{2 \sin \psi}{h^2} \frac{\partial \tilde{v}}{\partial \theta} \right), \end{aligned} \quad (3.2)$$

$$\begin{aligned} & \left( x\bar{U} \frac{\partial}{\partial x} + \frac{x\bar{V}}{h} \frac{\partial}{\partial \theta} + R^{-1/2} \bar{W} \frac{\partial}{\partial z} \right) \tilde{v} + \bar{V} \tilde{u} \\ & + x\tilde{w} \frac{\partial \bar{V}}{\partial z} + \left( \frac{x\bar{V} \sin \psi}{h} + 2 \right) (\tilde{u} + \tilde{w} \cot \psi) + \frac{(x\bar{U} \sin \psi + R^{-1/2} \bar{W} \cos \psi) \tilde{v}}{h} \\ & = -\frac{1}{h} \frac{\partial \tilde{p}}{\partial \theta} + \frac{1}{R} \left( \nabla^2 \tilde{v} + \frac{2 \sin \psi}{h^2} \frac{\partial \tilde{u}}{\partial \theta} + \frac{2 \cos \psi}{h^2} \frac{\partial \tilde{w}}{\partial \theta} - \frac{\tilde{v}}{h^2} \right), \end{aligned} \quad (3.3)$$

$$\begin{aligned} & \left( x\bar{U} \frac{\partial}{\partial x} + \frac{x\bar{V}}{h} \frac{\partial}{\partial \theta} + R^{-1/2} \bar{W} \frac{\partial}{\partial z} \right) \tilde{w} + R^{-1/2} \bar{w} \frac{\partial \bar{W}}{\partial z} - 2 \left( \frac{x\bar{V} \sin \psi}{h} + 1 \right) \tilde{v} \cot \psi \\ & = -\frac{\partial \tilde{p}}{\partial z} + \frac{1}{R} \left( \nabla^2 \tilde{w} - \frac{(\tilde{u} \sin \psi + \tilde{w} \cos \psi) \cos \psi}{h^2} - \frac{2 \cos \psi}{h^2} \frac{\partial \tilde{v}}{\partial \theta} \right), \end{aligned} \quad (3.4)$$

where  $h = x \sin \psi + z \cos \psi$  and

$$\nabla^2 = \frac{\partial^2}{\partial x^2} + \frac{1}{h^2} \frac{\partial^2}{\partial \theta^2} + \frac{\partial^2}{\partial z^2} + \frac{\sin \psi}{h} \frac{\partial}{\partial x} + \frac{\cos \psi}{h} \frac{\partial}{\partial z},$$

is the non-dimensional Laplacian operator.

### 3.2. Inviscid type I modes

To analyse the type I modes on the rotating cone, in accordance with Gregory *et al.* (1955) for the rotating disk, we scale the inviscid-mode wavelengths on the boundary-layer thickness, which is of order  $R^{-\frac{1}{2}}$ , in the  $x$ - and  $\theta$ -directions. A small parameter  $\epsilon$  can then be introduced, given by  $\epsilon = R^{-\frac{1}{6}}$ , and we subsequently define the perturbation velocities and pressure as functions of the wall-normal coordinate  $z$ , in the form

$$(\tilde{u}, \tilde{v}, \tilde{w}, \tilde{p}) = (u_A(z), v_A(z), w_A(z), p_A(z)) \exp\left(\frac{i}{\epsilon^3} \left\{ \int^x \alpha_A(x, \epsilon) dx + \beta_A(\epsilon) \theta \right\}\right).$$

We expand the streamwise and azimuthal wavenumbers as

$$\begin{aligned} \alpha_A &= \alpha_0 + \epsilon \alpha_1 + \dots, \\ \beta_A &= \beta_0 + \epsilon \beta_1 + \dots \end{aligned}$$

Significantly, we note that the disturbances associated with these perturbations are neutrally stable and hence  $\alpha_A$  and  $\beta_A$  are considered as real quantities. Note also that in this frame of reference the assumption of stationary vortices means that the disturbances have no time dependence.

Upon balancing convection and diffusion terms in the disturbance equations, we find the existence of two layers: an inviscid layer of thickness  $O(\epsilon^3)$  and a viscous layer to incorporate the no-slip condition at the wall, of thickness  $O(\epsilon^4)$ . The velocity and pressure

perturbations in the inviscid layer are expanded as

$$\begin{aligned} u_A &= u_0(\zeta) + \epsilon u_1(\zeta) + \dots, \\ v_A &= v_0(\zeta) + \epsilon v_1(\zeta) + \dots, \\ w_A &= w_0(\zeta) + \epsilon w_1(\zeta) + \dots, \\ p_A &= p_0(\zeta) + \epsilon p_1(\zeta) + \dots, \end{aligned}$$

where  $\zeta = z\epsilon^{-3}$ , consistent with equation (2.1). Here,  $\frac{\partial}{\partial x}$  and  $\frac{\partial}{\partial \theta}$  are replaced by  $\frac{\partial}{\partial x} + \frac{i}{\epsilon^3}\{\alpha_0 + \epsilon\alpha_1 + \dots\}$  and  $\frac{i}{\epsilon^3}\{\beta_0 + \epsilon\beta_1 + \dots\}$ , respectively.

### 3.2.1. Leading order and first order eigenmodes

We equate terms of  $O(\epsilon^{-3})$  in the expansions of equations (3.1)–(3.4), which leads to the governing Rayleigh equation in the critical layer for the surface-normal eigenfunction

$$\overline{\overline{U}}(w_0'' - \gamma_0^2 w_0) - \overline{\overline{U}}'' w_0 = 0, \quad (3.5)$$

with boundary conditions

$$\begin{aligned} w_0 &= 0, \quad \zeta = 0, \\ w_0 &\rightarrow 0, \quad \zeta \rightarrow \infty. \end{aligned} \quad (3.6)$$

Here  $\gamma_0^2 = \alpha_0^2 + \frac{\beta_0^2}{x^2 \sin^2 \psi}$ , which acts as the effective wavenumber from the streamwise and cross-stream directions, whereas  $\overline{\overline{U}} = \alpha_0 x \bar{U} + \frac{\beta_0 \bar{V}}{\sin \psi}$  is interpreted as the effective velocity profile, as discussed in a similar form by Hall (1986) for the rotating disk.

We solve equation (3.5) subject to the homogenous boundary conditions (3.6) by determining  $\zeta = \bar{\zeta}$  such that  $\overline{\overline{U}}$  and  $\overline{\overline{U}}''$  both vanish at the location of the critical layer,  $\zeta = \bar{\zeta}$ . Mathematically, we note that the important differences with respect to Hall's analysis are the radial coordinate  $r$ , which is now interpreted as the streamwise distance,  $x$ , and the azimuthal wavenumber is now scaled on the cone half-angle in terms of  $\beta_A/\sin \psi$ . Physically,  $\overline{\overline{U}}$  is in the direction of propagation of the spiral vortices on the rotating cone. To interpret this in more detail, we consider the rotating cone surface depicted in figure 2, noticing that the spiral vortices which wrap around the cone travel at an angle to the cone meridian. The streamwise and cross-stream wavenumbers,  $\alpha_0$  and  $\beta_0/r$ , are shown in the accompanying diagram of figure 2, with the normal to the spiral vortices in the direction of the effective velocity,  $\overline{\overline{U}}$ , making a waveangle,  $\phi$ , with the streamwise position vector.

Full details of the analysis are omitted here, but the reader is referred to Hall (1986) for a complete discussion. In brief, we asymptotically match the leading order eigensolution in the viscous wall layer to the first-order solution in the inviscid critical layer to obtain the governing eigenrelation

$$\frac{w_0'(0)^2 \text{Ai}'(0)}{\bar{\gamma} \int_0^\infty \text{Ai}(s) ds} = 2 \left( \alpha_0 \alpha_1 + \frac{\beta_0 \beta_1}{x^2 \sin^2 \psi} \right) I_1 + \left( \frac{\alpha_1}{\beta_0} - \frac{\beta_1 \alpha_0}{\beta_0^2} \right) \sin \psi x I_2, \quad (3.7)$$

where Ai is the Airy function,  $\bar{\gamma} = (i(\alpha_0 x \bar{U}'(0) + \frac{\beta_0 \bar{V}'(0)}{\sin \psi}))^{\frac{1}{3}}$  and we normalise the Rayleigh eigenfunction such that  $w_0'(0) = 1$ . The integrals  $I_1$  and  $I_2$  are identical to those defined in Hall (1986), and we obtain  $I_1 = 0.094$ ,  $I_2 = 0.058 + 0.029i$ . Note that the sign of the imaginary part of  $I_2$  differs from that given by Hall. Analysis of the flow within the critical layer reveals a phase jump in the surface-normal velocity perturbation, as

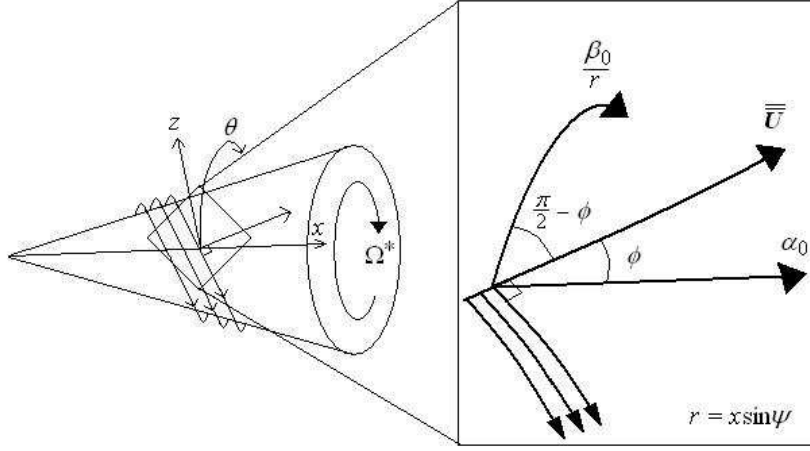


FIGURE 2. Schematic diagram of spiral vortex instability of a rotating cone (left) and the detailed physical interpretation (right) showing streamwise, azimuthal and effective velocity directions. Note the cone is rotating anti-clockwise when viewed from the nose tip.

a result of the integration contour being deformed above the singularity at  $\zeta = \bar{\zeta}$  (see Gajjar (2007)).

### 3.2.2. Type I asymptotic wavenumber and waveangle estimates

Upon solving eigenrelation (3.7) in terms of real and imaginary parts, we arrive at the leading-order and next-order corrections to the effective wavenumber

$$\begin{aligned}
 \gamma_{\delta^*} &= \left( \alpha_A^2 + \frac{\beta_A^2}{x^2 \sin^2 \psi} \right)^{\frac{1}{2}} \\
 &= \gamma_0 + \left( \alpha_0 \alpha_1 + \frac{\beta_0 \beta_1}{x^2 \sin^2 \psi} \right) \epsilon / \gamma_0 + \dots, \\
 &= 1.16 - 9.2 R_{\delta^*}^{-1/3} (\sin \psi)^{1/6} + \dots,
 \end{aligned} \tag{3.8}$$

as well as the spiral waveangle,

$$\begin{aligned}
 \tan \left( \frac{\pi}{2} - \phi \right) &= \frac{\alpha_A x}{\beta_A} \\
 &= \frac{\alpha_0 x}{\beta_0} + \left( \frac{\alpha_1}{\beta_0} - \frac{\beta_1 \alpha_0}{\beta_0^2} \right) x \epsilon + \dots, \\
 &= \frac{4.26}{\sin \psi} + 17.5 R_{\delta^*}^{-1/3} (\sin \psi)^{-\frac{5}{6}} + \dots
 \end{aligned} \tag{3.9}$$

$R_{\delta^*}$  is the Reynolds number based on the boundary-layer thickness,  $\delta^* = (\nu^* / \Omega^*)^{\frac{1}{2}}$  given by

$$R_{\delta^*} = R^{\frac{1}{2}} x (\sin \psi)^{\frac{1}{2}}. \tag{3.10}$$

Figures 3 and 4 show the inviscid branches of the neutral curves for the asymptotic wavenumber and waveangle predictions, given respectively in equations (3.8, 3.9), for  $\psi = 20^\circ - 90^\circ$  in  $10^\circ$  increments. From these we can see that increasing the cone half-angle stabilizes the flow by rendering less wavenumbers susceptible to the instability. For

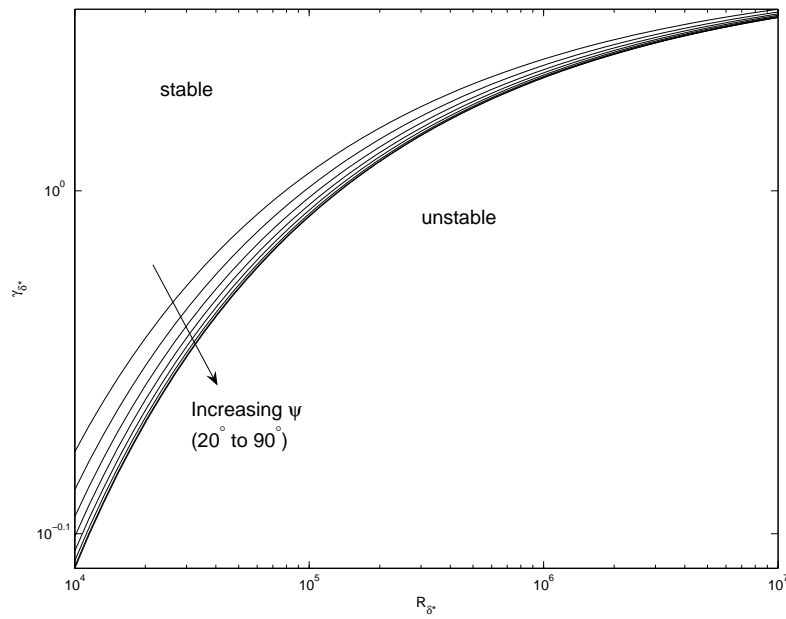


FIGURE 3. Neutral asymptotic wavenumber predictions,  $\gamma_{\delta^*}$ , for inviscid (type I) modes as a function of  $R_{\delta^*}$  for  $\psi = 20^\circ - 90^\circ$ .

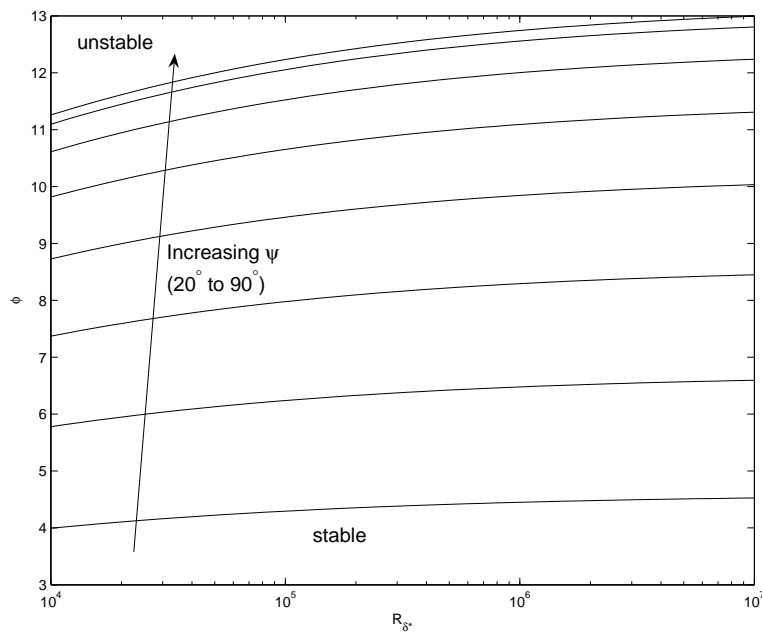


FIGURE 4. Neutral asymptotic waveangle predictions,  $\phi$ , for inviscid (type I) modes as a function of  $R_{\delta^*}$  for  $\psi = 20^\circ - 90^\circ$ .



the waveangle, increasing the half-angle towards that of a rotating disk has the effect of deviating the spiral vortices more from the streamwise direction. Physically this is plausible, as there is an increased ‘rotational shear’ force on each vortex spiral as the cone’s gradient of slant increases with  $\psi$ ; vortices are therefore deviated more from the streamwise direction.

Interpreting the results in terms of energy transfer: on a rotating disk the vortices transfer less energy in the radial direction than in the azimuthal direction (due to the purely rotational effect of the disk) and so the resulting deviation waveangle is relatively large. For a rotating cone of a moderate to slender half-angle, the streamline-curvature effect of the cone surface causes the spiral vortices to transfer more energy in the streamwise direction. This aligns the direction of the effective velocity propagation more with the streamwise vector, resulting in a reduction in the observed waveangle. However, this is not the case for the wavenumber as the effective vorticity shed from the cone boundary layer does not change substantially with half-angle, which means that the number of vortices that are observed to roll-up and wrap around the cone surface are of the same order.

### 3.3. Viscous type II modes

In this section we consider the stability of stationary viscous modes to lower-branch disturbances using a triple-deck structure consistent with Hall (1986) on the rotating disk and analogous to that found for Blasius flow over a flat-plate (see Smith (1979)).

We take the triple-deck structure to be built on a small parameter, which is now given by  $\epsilon = R^{-\frac{1}{16}}$ , with the lower, main and upper decks typically having thicknesses of order  $\epsilon^9$ ,  $\epsilon^8$  and  $\epsilon^4$ , respectively. We define inner variables  $\xi$ ,  $\zeta$ , and  $Z$  to represent  $O(1)$  variation within the lower, main and upper decks, respectively. In line with Hall’s formulation, the streamwise and azimuthal wavenumbers,  $\alpha_A$  and  $\beta_A$ , are scaled upon a viscous length-scale, so that the velocity and pressure perturbations become

$$(\tilde{u}, \tilde{v}, \tilde{w}, \tilde{p}) = (u_A(z), v_A(z), w_A(z), p_A(z)) \exp\left(\frac{i}{\epsilon^4} \left\{ \int^x \alpha_A(x, \epsilon) dx + \beta_A(\epsilon) \theta \right\}\right).$$

We now expand the streamwise and azimuthal wavenumbers as

$$\begin{aligned} \alpha_A &= \alpha_0 + \epsilon^2 \alpha_1 + \epsilon^3 \alpha_2 + \dots, \\ \beta_A &= \beta_0 + \epsilon^2 \beta_1 + \epsilon^3 \beta_2 + \dots, \end{aligned}$$

noting that the  $O(\epsilon)$  terms are zero, and  $\alpha_i$  and  $\beta_i$  (where  $i = 0, 1, 2, \dots$ ) are real quantities. As was the case with the type I modes, much of the analysis for the wall-dominated type II modes for the rotating cone transpires to be very similar to the rotating-disk wall modes studied by Hall, with the important difference of a scale factor  $\sin \psi$ .

#### 3.3.1. Triple-deck analysis

We investigate the boundary-layer structure by obtaining leading order solutions in each of the decks. In the upper deck, disturbances decay exponentially, whereas in the main deck we use the no-slip condition to argue that the effective wall shear tends to zero as  $\zeta \rightarrow 0$ . We therefore choose the leading order streamwise and azimuthal wavenumbers such that

$$\alpha_0 \bar{U}'(0) + \frac{\beta_0}{x \sin \psi} \bar{V}'(0) = 0. \quad (3.11)$$

Finally, in the lower deck, the decay of the leading order solution is manifested in terms of the parabolic cylinder function  $U(0, \sqrt{2\Delta}^{\frac{1}{4}} \xi)$  (see Abramowitz & Stegun (1964))

through the balance of viscous and Coriolis forces. Here we have

$$\Delta = i\left(\alpha_0 x U_1 + \frac{\beta_0}{\sin \psi} V_1\right),$$

where  $U_{i-1} = \bar{U}^{(i)}(0)/i!$  and  $V_{i-1} = \bar{V}^{(i)}(0)/i!$  for  $i = 1, 2, \dots$ . These solutions are matched with the first-order solution in the lower deck to arrive at the eigenrelation

$$\gamma_0^2 I_3 + \frac{i\gamma_0 U_0 \sin \psi}{\beta_0} \left(1 + \frac{V_0^2}{U_0^2}\right) I_4 = \frac{i\Delta^{\frac{1}{2}} \gamma_0 \sin^2 \psi}{\beta_0^2} \left(\alpha_1 x U_0 + \frac{\beta_1 V_0}{\sin \psi}\right), \quad (3.12)$$

where  $I_3$  and  $I_4$  are integrals involving  $U(0, \theta)$  defined in Hall (1986) and the leading order effective wavenumber is given by  $\gamma_0 = \sqrt{\left(\alpha_0^2 + \frac{\beta_0^2}{x^2 \sin^2 \psi}\right)}$ . We obtain the values  $I_3 = 0.599$ ,  $I_4 = 0.457$  consistent with those calculated by Hall.

### 3.3.2. Type II asymptotic wavenumber and waveangle estimates

As in §3.2.2, the eigenrelation (3.12) has been decomposed into real and imaginary parts and solved to yield estimates for the local asymptotic wavenumber and waveangle, given by

$$\begin{aligned} \gamma_{\delta^*} &= \left(\alpha_A^2 + \frac{\beta_A^2}{x^2 \sin^2 \psi}\right)^{\frac{1}{2}} R^{-\frac{1}{4}} \\ &= \left(1 + \frac{V_0^2}{U_0^2}\right)^{\frac{3}{4}} \left(\frac{U_0 I_4}{I_3}\right)^{\frac{1}{2}} x^{-\frac{1}{2}} R^{-\frac{1}{4}} \\ &= 1.22 R_{\delta^*}^{-\frac{1}{2}} (\sin \psi)^{\frac{1}{4}} + \dots \end{aligned} \quad (3.13)$$

and

$$\begin{aligned} \tan\left(\frac{\pi}{2} - \phi\right) &= \frac{\alpha_A x}{\beta_A} \\ &= \frac{(\alpha_0 + \epsilon^2 \alpha_1 + \dots)x}{(\beta_0 + \epsilon^2 \beta_1 + \dots)}, \\ &= \frac{\alpha_0 x}{\beta_0} + \epsilon^2 \left(\frac{\alpha_1}{\beta_0} - \frac{\beta_1 \alpha_0}{\beta_0^2}\right)x, \\ &= \frac{1.21}{\sin \psi} + 2.31 R_{\delta^*}^{-\frac{1}{4}} (\sin \psi)^{-\frac{7}{8}} + \dots \end{aligned} \quad (3.14)$$

Again, we re-scale the wavenumber and waveangle in terms of the Reynolds number based on boundary layer-thickness (equation (3.10)); this eliminates any dependence of the estimates on the streamwise location  $x$ .

Figures 5 and 6 show the lower branches of the neutral curve for the asymptotic wavenumber and waveangle predictions. In a similar fashion to the inviscid branch, we see that increasing the cone half-angle has the effect of stabilizing the flow by reducing the available wavenumbers which are susceptible to the instability. Furthermore, in the case of the waveangle, increasing the cone half-angle towards that of a rotating disk still has the effect of increasing the waveangle, which we interpret physically as a consequence of the rotational shear forcing effect detailed in §3.2.2.

Comparisons of our wall-mode results, together with those for the inviscid modes in §3.2, reveals a greater variation in the asymptotic estimates of the waveangle with  $\psi$ , than for the corresponding wavenumber. We attribute this feature to our choice of

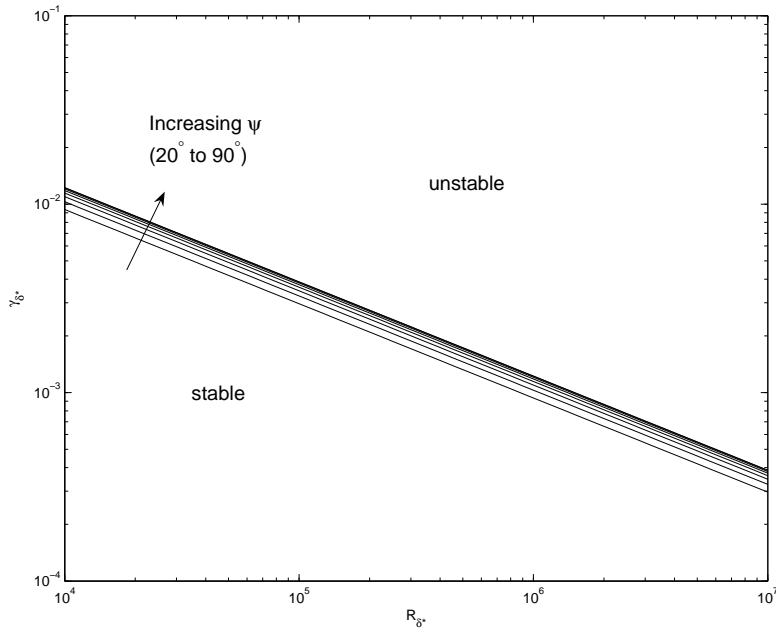


FIGURE 5. Neutral asymptotic wavenumber predictions,  $\gamma_{\delta^*}$ , for viscous (type II) modes as a function of  $R_{\delta^*}$  for  $\psi = 20^\circ - 90^\circ$ .

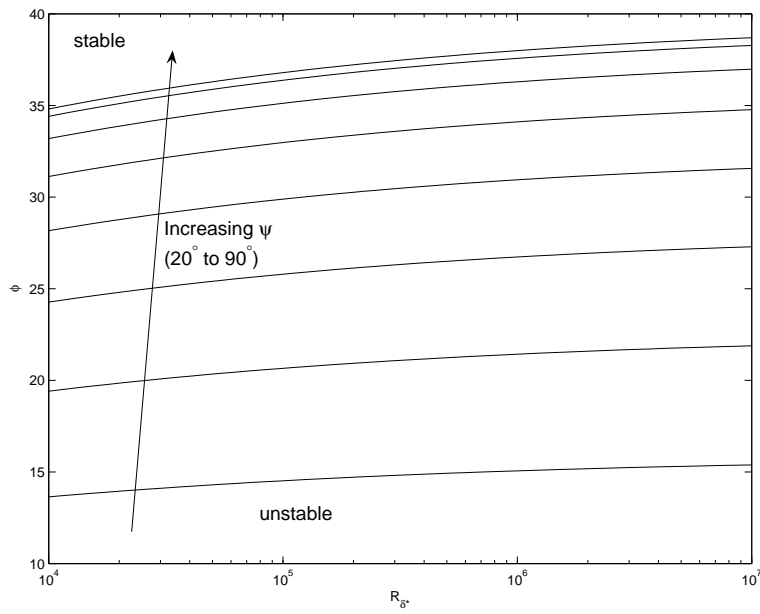


FIGURE 6. Neutral asymptotic waveangle predictions,  $\phi$ , for viscous (type II) modes as a function of  $R_{\delta^*}$  for  $\psi = 20^\circ - 90^\circ$ .

non-dimensionalisation: scaling lengths on the distance along the cone,  $l^*$ , eliminates dependence of the leading order wavenumber,  $\gamma_0$ , on  $\psi$ .

The rightmost wavenumber curve and uppermost waveangle curve for both type I and type II disturbances correspond to  $\psi = 90^\circ$  and agrees well with the results of Hall (1986), as well as with the numerical results of Malik (1986) for a rotating disk.

## 4. Numerical study

### 4.1. Linear disturbance equations for the numerical analysis

For the numerical study we use slightly different scalings to those introduced in §2, based on the length scale provided by the boundary-layer thickness  $\delta^* = (\nu^*/\Omega^*)^{1/2}$ . For simplicity the notation used in this section is consistent with that used in the asymptotic study for equivalent quantities, although the non-dimensionalisations are different. Care should therefore be taken in any comparisons made with previous sections. We also consider the cone to be rotating in a fixed frame of reference. This formulation is consistent with Garrett & Peake (2007) and permits investigation of the speed at which vortices rotate with respect to the cone body. This frame of reference necessarily eliminates the appearance of Coriolis terms in the governing equations.

The numerical stability analysis is conducted at local points along the cone surface  $x^* = x_L^*$ , where the local surface radius is  $r_L^* = x_L^* \sin \psi$ . The non-dimensionalising length, velocity, pressure and time scales are  $\delta^*$ ,  $r_L^* \Omega^*$ ,  $\rho^* r_L^{*2} \Omega^{*2}$  and  $\delta^*/\Omega r_L^*$  respectively, which lead to the local Reynolds number

$$R_L = \frac{x_L^* \Omega^* \sin \psi \delta^*}{\nu^*} = x_L \sin \psi = r_L, \quad (4.1)$$

which differs from the Reynolds number used in (2.4) of the asymptotic study. However, we have  $R_L = R_{\delta^*}$ , the displacement-thickness Reynolds number defined in (3.10).

The resulting steady mean flow equations are identical to those presented by Garrett & Peake (2007) (equations (2)–(5)) when  $T_s = 0$ . These differ from equations (2.5)–(2.9) through the appearance of  $\sin \psi$  factors and the non-appearance of Coriolis terms. The numerical study is therefore conducted for each  $\psi$ , and the basic flow quantities  $U(\eta; \psi)$ ,  $V(\eta; \psi)$  and  $W(\eta; \psi)$  are necessarily different to those presented in §2. Note also that  $\eta = z^*/\delta^*$  so  $\eta = \zeta/(\sin \psi)^{1/2}$ .

In order to derive the disturbance equations we consider the instantaneous non-dimensional flow quantities to be given by

$$\begin{aligned} \tilde{U}(\eta, x, \theta, t; R_L, \psi) &= \frac{r}{R_L} U(\eta; \psi) + \hat{u}(\eta, x, \theta, t; R_L, \psi), \\ \tilde{V}(\eta, x, \theta, t; R_L, \psi) &= \frac{r}{R_L} V(\eta; \psi) + \hat{v}(\eta, x, \theta, t; R_L, \psi), \\ \tilde{W}(\eta, x, \theta, t; R_L, \psi) &= \frac{1}{R_L} W(\eta; \psi) + \hat{w}(\eta, x, \theta, t; R_L, \psi), \\ \tilde{P}(\eta, x, \theta, t; R_L, \psi) &= \frac{1}{R_L^2} P(\eta; \psi) + \hat{p}(\eta, x, \theta, t; R_L, \psi), \end{aligned}$$

where the hatted quantities are small unsteady perturbations and the unhatted quantities are the non-dimensional flow determined by modified forms of equations (2.5)–(2.7), as discussed above. The non-dimensional continuity and Navier–Stokes equations are linearized with respect to these perturbation quantities and the parallel-flow approximation is made.

In applying the parallel-flow approximation we ignore variation in  $R_L$  with local surface

cross-sectional radius and assume that  $\eta/r_L \ll 1$ . The resulting stability equations are then strictly local, with location  $R_L = r_L$  appearing as a parameter. The assumption that  $R_L \gg 1$  (equivalent to  $\delta^* \ll x_L^*$ ) necessarily prohibits analysis close to the apex where  $R_L = O(1)$ . The perturbation quantities can then be expressed in normal-mode form

$$(\hat{u}, \hat{v}, \hat{w}, \hat{p}) = (u(\eta; \psi), v(\eta; \psi), w(\eta; \psi), p(\eta; \psi)) \exp(i(\alpha x + \beta R_L \theta - \gamma t)).$$

The wavenumber in the  $x$ -direction,  $\alpha = \alpha_r + i\alpha_i$ , is complex as required by the spatial analysis presented here; the frequency,  $\gamma$ , and circumferential wavenumber,  $\beta$ , are real. It is assumed that  $\beta$  is  $O(1)$ .

The integer number of complete cycles of the disturbance round the azimuth is  $n = \beta R_L$ , and we identify this with the number of spiral vortices. We also note that the disturbance phase velocity in the azimuthal direction is  $c = \gamma/\beta$ , we identify this as the speed at which the vortices rotate with respect to the cone surface. This is equivalent to the analysis presented in Garrett & Peake (2002) and Garrett & Peake (2004) for the rotating sphere; further details can be found in those papers.

As in Garrett & Peake (2007), the perturbation quantities may be written as a set of six first-order ordinary-differential equations using the transformed variables: †

$$\begin{aligned} \phi_1 &= (\alpha - i \sin \psi / R_L) u + \beta v, & \phi_2 &= (\alpha - i \sin \psi / R_L) u' + \beta v', & \phi_3 &= w \\ \phi_4 &= p, & \phi_5 &= (\alpha - i \sin \psi / R_L) v - \beta u, & \phi_6 &= (\alpha - i \sin \psi / R_L) v' - \beta u'. \end{aligned}$$

These equations are

$$\phi_1' = \phi_2, \tag{4.2}$$

$$\begin{aligned} \left[ \frac{\phi_2'}{R_L} \right]_v &= \frac{1}{R_L} \left( [\alpha^2 + \beta^2]_v + i R_L (\alpha U + \beta V - \gamma) + [U \sin \psi]_s \right) \phi_1 \\ &+ \left[ \frac{W \phi_2}{R_L} \right]_s + \left( \left( \alpha - \left[ \frac{i \sin \psi}{R_L} \right]_s \right) U' + \beta V' \right) \phi_3 \\ &+ i \left( \alpha^2 + \beta^2 - \left[ \frac{i \alpha}{R_L} \right]_s \right) \phi_4 - \left[ \frac{2V \sin \psi \phi_5}{R_L} \right]_s, \end{aligned} \tag{4.3}$$

$$\phi_3' = -i \phi_1 - \left[ \frac{\phi_3 \cos \psi}{R_L} \right]_s, \tag{4.4}$$

$$\begin{aligned} \phi_4' &= \left[ \frac{iW \phi_1}{R_L} \right]_s - \left[ \frac{i \phi_2}{R_L} \right]_v \\ &- \frac{1}{R_L} \left( [\alpha^2 + \beta^2]_v + i R_L (\alpha U + \beta V - \gamma) + W'_s \right) \phi_3, \end{aligned} \tag{4.5}$$

$$\phi_5' = \phi_6, \tag{4.6}$$

$$\begin{aligned} \left[ \frac{\phi_6'}{R_L} \right]_v &= \left[ \frac{2V \sin \psi \phi_1}{R_L} \right]_s + \left( \left( \alpha - \left[ \frac{i \sin \psi}{R} \right]_s \right) V' - \beta U' \right) \phi_3 \\ &+ \frac{1}{R_L} \left( [\alpha^2 + \beta^2]_v + i R_L (\alpha U + \beta V - \gamma) + [U \sin \psi]_s \right) \phi_5 \\ &+ \left[ \frac{\beta \sin \psi \phi_4}{R_L} \right]_s + \left[ \frac{W \phi_6}{R_L} \right]_s, \end{aligned} \tag{4.7}$$

† We wish to point out a typographical error in Garrett & Peake (2007) by noting that the correct signs in the definition of  $\phi_5$  and  $\phi_6$  are as given here.

where the subscripts  $v$  and  $s$  indicate which of the  $O(R_L^{-1})$  terms arise from the viscous and streamline-curvature effects respectively.

The streamline-curvature terms represent the effect of deflection of the inviscid-flow streamlines through the action of the pressure gradient. By neglecting these terms in (4.2)–(4.7), the system of equations is demonstrated to be consistent with the Orr–Sommerfeld equation for the rotating cone in the form

$$\begin{aligned} (i/R_L)(\phi_3'''' - 2(\alpha^2 + \beta^2)\phi_3'' + (\alpha^2 + \beta^2)^2\phi_3) \\ + (\alpha U + \beta V - \gamma)(\phi_3'' - (\alpha^2 + \beta^2)\phi_3) - (\alpha U'' + \beta V'')\phi_3 = 0. \end{aligned} \quad (4.8)$$

Further, neglecting both the streamline-curvature and viscous terms in the perturbation equations leads to Rayleigh’s equation in the form

$$(\alpha U + \beta V - \gamma)(\phi_3'' - (\alpha^2 + \beta^2)\phi_3) - (\alpha U'' + \beta V'')\phi_3 = 0. \quad (4.9)$$

Although solutions of equations (4.8) and (4.9) will be mentioned briefly, the focus of this study is the solution of the full equations (4.2)–(4.3).

#### 4.2. Numerical solution

In this section we solve the eigenvalue problem defined by (4.2)–(4.7), with the homogenous boundary conditions

$$\begin{aligned} \phi_i = 0, \quad \eta = 0, \\ \phi_i \rightarrow 0, \quad \eta \rightarrow \infty, \end{aligned}$$

where  $i = 1, 2 \dots 6$ . This eigenvalue problem will be solved for certain combinations of values of  $\alpha$ ,  $\beta$  and  $\gamma$  at each Reynolds number,  $R_L$ , and for a particular value of  $\psi$ . From these we form the dispersion relation,  $D(\alpha, \beta, \gamma; R_L, \psi) = 0$ , at each  $\psi$ , with the aim of studying the occurrence of convective instabilities. This method is in contrast to that presented by Kobayashi & Izumi (1983) where a temporal analysis is formulated in terms of the waveangle.

In what follows the spatial branches are calculated using a double-precision fixed-step-size, fourth-order Runge–Kutta integrator with Gram–Schmidt orthonormalization and a Newton–Raphson linear search procedure, using the numerical code discussed in Garrett (2002).

##### 4.2.1. Stationary vortices

We begin by explicitly assuming that the vortices rotate with the surface of the cone, i.e.  $c = 1.0$  and so  $\gamma = \beta$ , which is consistent with the experimental observations described in §1. We provide a theoretical justification of this approach in §4.2.2. The term *stationary vortices* is used to distinguish between vortices that rotate with the surface of the cone and *non-stationary vortices* that do not.

In order to investigate the spatial branches at each half-angle, we solve the dispersion relation for  $\alpha$  whilst marching through values of  $\gamma = \beta$  at fixed  $R_L$ . For each  $\psi$  we find that two spatial branches determine the convective-instability characteristics of the system. Figure 7(a) shows these two branches in the complex  $\alpha$ -plane when  $\psi = 70^\circ$  and  $R_L = 400$ . A branch lying below the  $\alpha_r$ -axis indicates convective instability. In the analysis of the Orr–Sommerfeld equation (4.8), branch 2 is not found indicating that it arises from streamline-curvature effects. Branch 1 is present in the analyses of the Orr–Sommerfeld and Rayleigh’s (4.9) equations and so arises from inviscid crossflow effects.

Figure 7(b) shows the two branches when  $\psi = 70^\circ$  and  $R_L = 437$  and we see that an exchange of modes has occurred between them. The modified branch 1 now determines the region of convective instability. Increasing the value of  $R_L$  further causes the peak

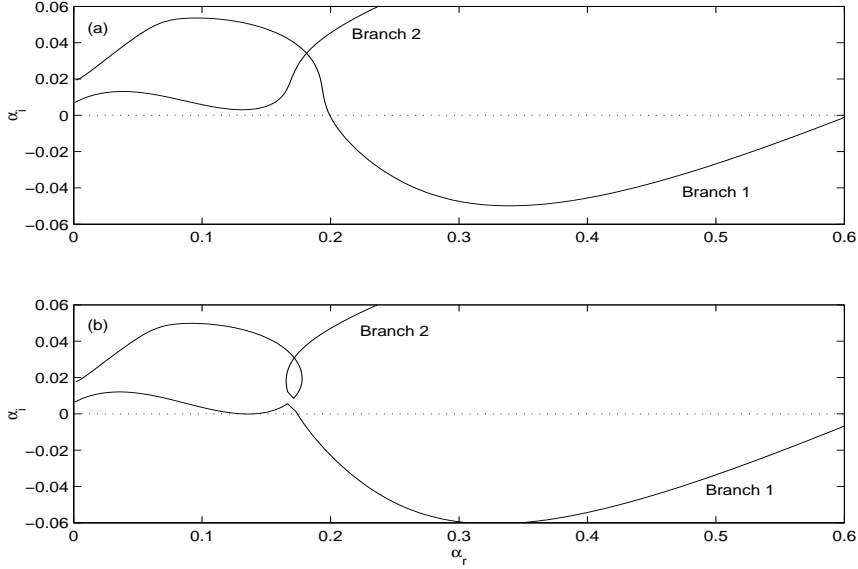


FIGURE 7. The two spatial branches for  $\psi = 70^\circ$  showing (a) type I instability from branch 1 only at  $R_L = 400$ ; (b) type I and type II instability from the modified branch 1 at  $R_L = 437$ .

between the two minima on the modified branch 1 to move downwards and the points where the branch crosses the  $\alpha_r$ -axis to move apart, thereby widening the two regions of instability mapping out two lobes on the neutral curve. Above a certain value of  $R_L$  the peak moves below the  $\alpha_r$ -axis and further increases in  $R_L$  change the region of instability producing the upper and lower branches of the neutral curve. We identify the crossflow mode as the type I instability and the streamline-curvature mode as the type II instability in this frame of reference.

This behaviour of the spatial branches is typical for all  $\psi$ , and neutral curves (defined by  $\alpha_i = 0$ ) have been calculated for half-angles between  $\psi = 20^\circ$ – $90^\circ$  in increments of  $10^\circ$ . Neutral curves based on these results are shown in §5, where a characteristic two-lobed structure is apparent (see Garrett (2002) for further details). The neutral curve for  $\psi = 90^\circ$  is identical to that calculated by Malik (1986).

#### 4.2.2. Non-stationary vortices

To investigate the longitudinal vortex speed we take a different approach in solving the dispersion relation: we plot spatial branches for fixed values of  $n$  (equivalent to fixing  $\beta$  at each particular  $R_L$ ) and march through values of  $\gamma$ . The global neutral curves for each  $\psi$  would then be the envelope of the individual neutral curves defined by  $\alpha_i = 0$  pertaining to each  $n$ . This approach does not require *a priori* knowledge of  $c$ , and allows it to be predicted from  $\gamma$  and  $n$  at the critical values of  $R_L$  using the relationship

$$c = \frac{\gamma R_L}{n}.$$

This approach has been taken for all half-angles investigated and figure 8 shows the enveloping curves in the region of the onset of instability for a number of these. In the range of  $n$  considered, we note that each curve has a single minimum (corresponding to the most dangerous type I mode) occurring when  $c \approx 1.0$  as demonstrated in table 1.

It is important to note that these results demonstrate that disturbances arising from the type I mode are almost stationary with respect to the cone surface. An alternative

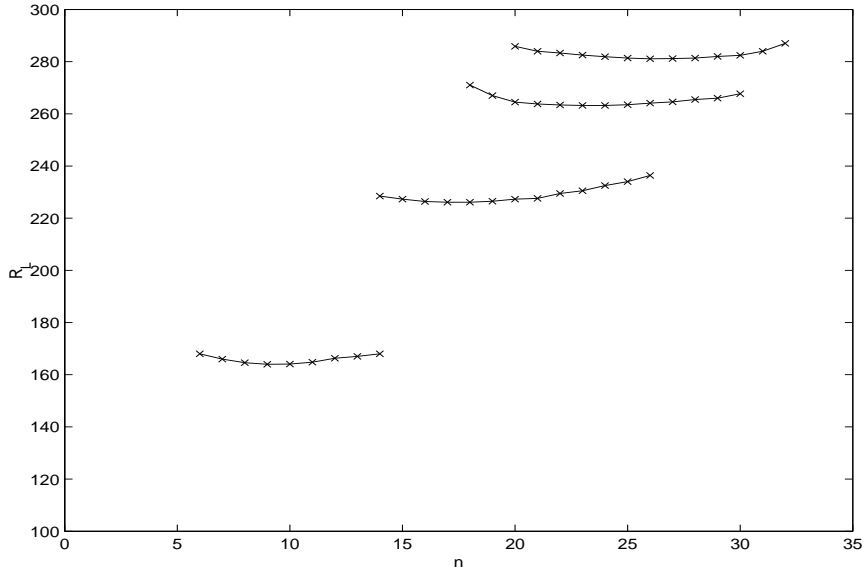


FIGURE 8. Critical values of  $R_L$  for  $\psi = 20^\circ\text{--}80^\circ$  in  $20^\circ$  increments (bottom to top) calculated by fixing  $n$  at various integer values.

---

$\psi$	$R_L$	$\gamma$	$n$	$c$
20	165.3	0.0475	8	0.982
40	228.3	0.0616	14	1.004
60	265.5	0.0711	19	0.993
80	283.6	0.0773	22	0.997

---

TABLE 1. Critical values of parameters for a range of half-angles calculated by fixing  $n$  at various integer values.

numerical investigation into the rotating disk boundary layer by Turkyilmazoglu & Gajjar (1998) appears to demonstrate that disturbances arising from the type II mode can move at different speeds relative to the disk surface, and with considerably lower critical Reynolds numbers than for the type I mode. Under their formulation in the rotating frame, the value of  $\gamma$  is fixed for each neutral curve plot and  $\beta$  is treated as an independent variable; fixing  $\gamma$  at different values then enables the analysis of vortices which rotate at different speeds relative to the disk surface.

#### 4.2.3. Effective wall shear

The effective wall shear along the lower branch is assumed to be zero in the asymptotic investigation of the type II mode presented in §3.3.1. This assumption is not necessary in the numerical formulation, but we are able to predict its value from the parameters along the type II branch of the neutral curves numerically calculated in §4.2.1.

The scalings used in the numerical formulation lead to the definition of effective wall shear as

$$\frac{\alpha U'(0; \psi) + \beta V'(0; \psi)}{\sin \psi},$$

which is consistent with the mathematical definition given in equation (3.11). This quan-



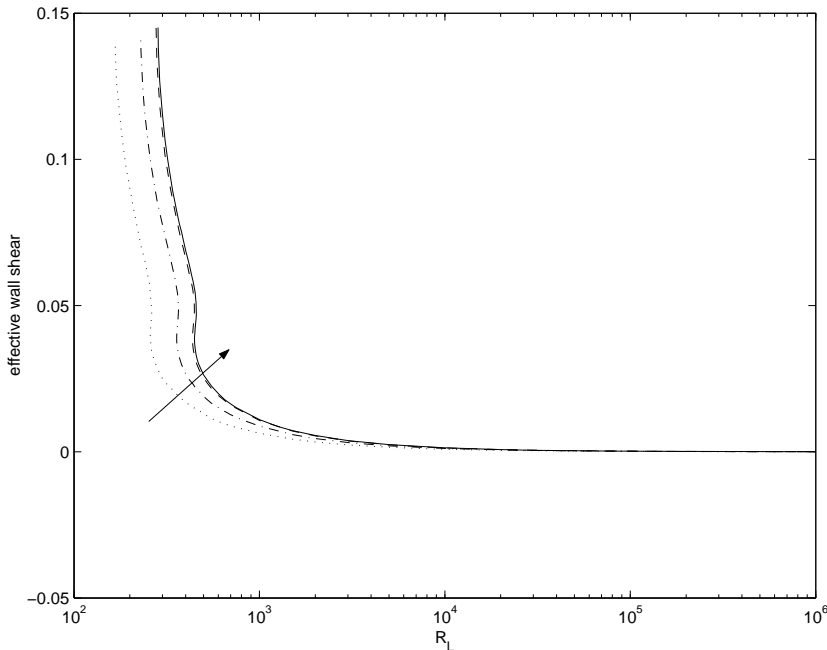


FIGURE 9. Numerical prediction of the effective wall shear along the type II branch for  $\psi = 20^\circ, 40^\circ, 70^\circ, 80^\circ$  (arrow indicates direction of increasing  $\psi$ ).

tity is plotted in figure 9 for a number of half-angles. We note that the effective wall shear does indeed tend to zero in each case as the Reynolds number increases, providing a justification of the assumption made in the asymptotic investigation.

## 5. Results and discussion

### 5.1. Comparison between the asymptotic and numerical investigations

We note that the local Reynolds number, equation (4.1), used in the numerical analysis can be immediately identified with the displacement-thickness Reynolds number defined by equation (3.10). Furthermore, a comparison of the respective normal mode perturbation structures between the asymptotic and numerical investigations reveal  $\alpha = \alpha_A (\sin \psi)^{\frac{1}{2}}$  and  $\beta = \beta_A / (x (\sin \psi)^{\frac{1}{2}})$ , where the subscript  $A$  denotes the asymptotic parameters, and numerical parameters remain undecorated. All quantities are considered real to ensure a consistent formulation with both analyses. We subsequently arrive at the following relations

$$k_\delta = \frac{1}{(\sin \psi)^{\frac{1}{2}}} (\alpha^2 + \beta^2)^{\frac{1}{2}}, \quad (5.1)$$

$$\epsilon = \arctan \left( \frac{\beta \sin \psi}{\alpha} \right), \quad (5.2)$$

which can be directly identified with the asymptotic predictions of wavenumber, equations (3.8, 3.13), and waveangle, equations (3.9, 3.14).

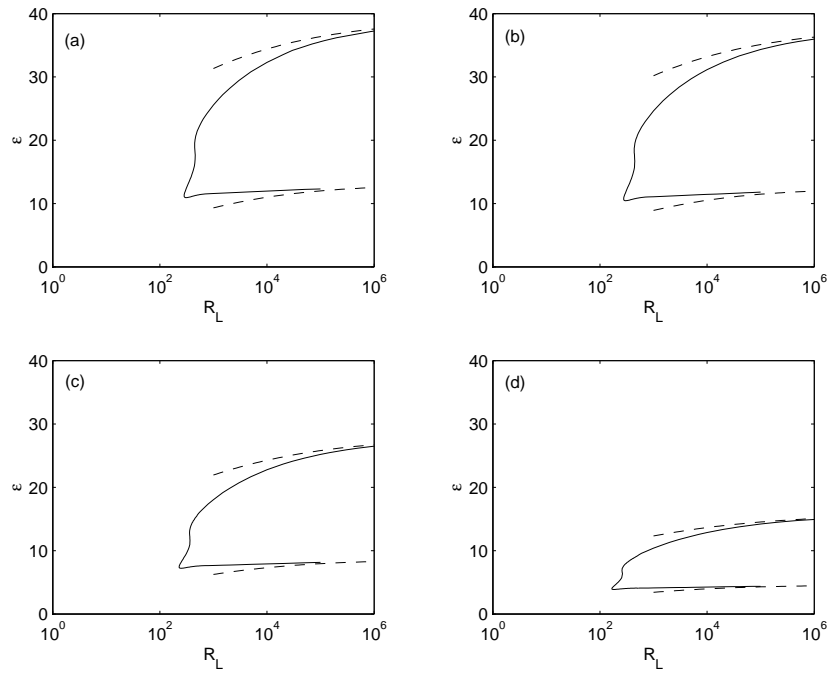


FIGURE 10. Neutral-stability curves for stationary modes in terms of predicted waveangle (solid line numerical, dashed line asymptotic) (a)  $\psi = 80^\circ$ ; (b)  $\psi = 70^\circ$ ; (c)  $\psi = 40^\circ$ ; (d)  $\psi = 20^\circ$ .

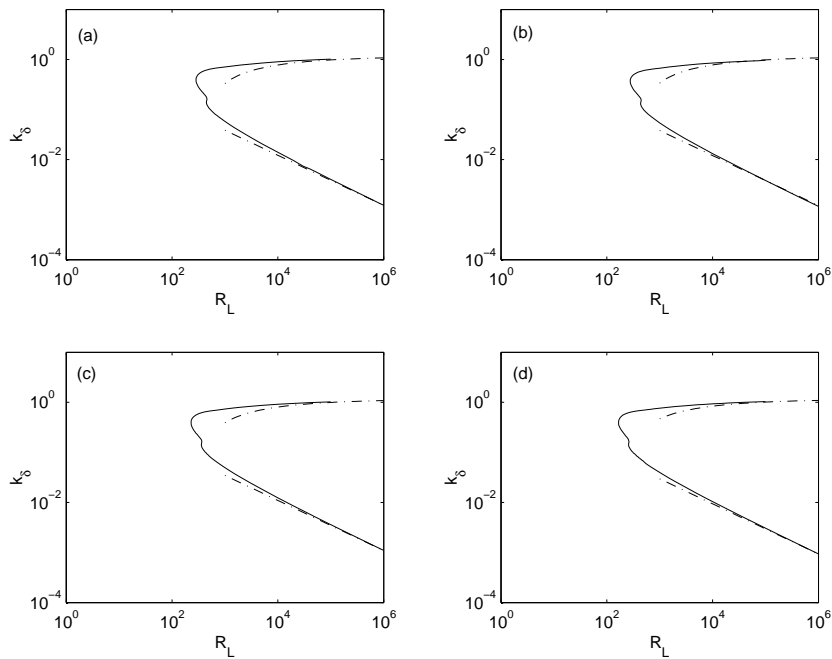


FIGURE 11. Neutral-stability curves for stationary modes in terms of predicted wavenumber (solid line numerical, dashed line asymptotic) (a)  $\psi = 80^\circ$ ; (b)  $\psi = 70^\circ$ ; (c)  $\psi = 40^\circ$ ; (d)  $\psi = 20^\circ$ .

Figure 10 shows a comparison between the numerically-calculated waveangle  $\epsilon$  and the asymptotic waveangle  $\phi$  for a number of half-angles. Excellent agreement has been found for both instability modes at all  $\psi$  between  $20^\circ$ – $90^\circ$ . Figure 11 shows the equivalent plot in terms of the numerically-calculated wavenumber  $k_\delta$  and asymptotic estimate  $\gamma_\delta^*$ . We have found excellent quantitative agreement for all  $\psi$  between  $20^\circ$ – $90^\circ$ . Qualitatively, we observe a decrease in  $\psi$  reduces both waveangle branches and also shifts the wavenumber neutral curves from right to left. Essentially, lower critical Reynolds numbers are obtained (as shown in figure 8), which results in an enlarged unstable region. Hence, decreasing  $\psi$  is found to destabilise the flow.

Similar comparisons for the rotating disk have been given recently for stationary and non-stationary neutral solutions by Turkyilmazoglu (2006, 2007).

### 5.2. Comparison with previous experimental studies

Figure 12 shows a comparison between the predicted onset of the two instability modes found in the numerical investigation for stationary vortices and the observed onset of spiral vortices as measured in three experimental investigations: Kreith *et al.* (1962); Kappesser *et al.* (1973) and Kobayashi & Izumi (1983). Note the use of the Reynolds number based on the local surface radius,  $Re = x^* \Omega^* \sin^2 \psi / \nu^* = R^2$ , used in the experimental investigations.

The predicted onset of the type I mode is seen to match Kobayashi & Izumi's measurements well for  $\psi \geq 60^\circ$ . However, the predicted onset deviates from these measurements as the half-angle is reduced. At  $\psi = 30^\circ$ , the predictions match the experimental measurements for Kreith *et al.* and Kappesser *et al.* reasonably well. For cones with half-angles between  $\psi = 30^\circ$ – $60^\circ$ , the predicted onset of the type I mode lies between the three sets of experimental data. The measurements conducted by Kappesser *et al.* are reasonably close to the predicted onset of the type II mode when  $\psi \geq 60^\circ$ .

These observations may suggest that Kappesser *et al.* were measuring the onset of the type II modes in their experiments on cones with large  $\psi$ , and the onset of the type I modes on the more slender cones. We also suggest that Kobayashi & Izumi were measuring the onset of a type I mode for large  $\psi$ , but some other mode on the slender cones. The oldest set of data, due to Kreith *et al.*, is inconsistent with all other data in figure 12 for  $\psi \geq 50^\circ$ ; we suggest that this is due to their experimental technique.

Although not shown here, solution of the Orr–Sommerfeld equation (4.8) leads to lower critical Reynolds numbers for the onset of stationary modes, as indicated in figure 2 of Lingwood (1995) for the rotating disk. The solution of the full perturbation equations (4.2)–(4.7) is therefore preferred.

Figure 13 shows a comparison between Kobayashi & Izumi's experimental waveangles and those predicted by the asymptotic and numerical investigations for the more dangerous type I mode. The critical  $R$  numerical prediction refers to the onset of type I instability, whereas the asymptotic values are at large  $R$  (typically  $O(10^6)$ ). We observe reasonable agreement when  $\psi \geq 40^\circ$ . It is likely that the small quantitative discrepancy in this regime exists because we necessarily assume that the vortices are neutrally stable, however they are experimentally observed to be growing in the streamwise direction.

As  $\psi$  is decreased below  $40^\circ$ , the theoretical predictions deviate from experimental results. We attribute this behaviour to the change in the underlying instability observed by Kobayashi & Izumi (1983). This is consistent with the suggestions of Kobayashi (1994) and Kohama (2000), who identified  $\psi = 30^\circ$  as the possible transition case from co-rotating to counter-rotating vortices.

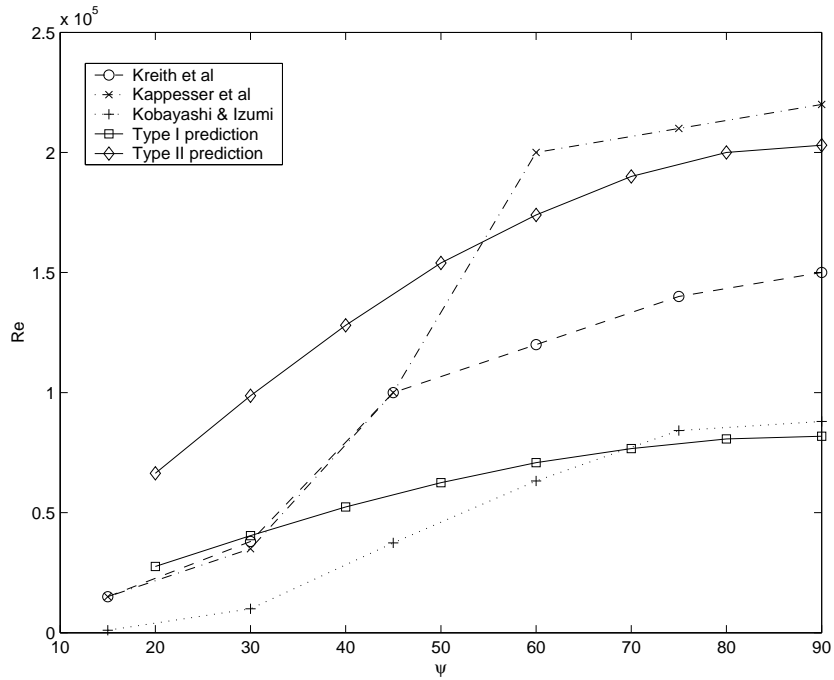


FIGURE 12. A comparison of the numerically calculated critical Reynolds number for the onset of each stationary instability mode with experimental measurements.

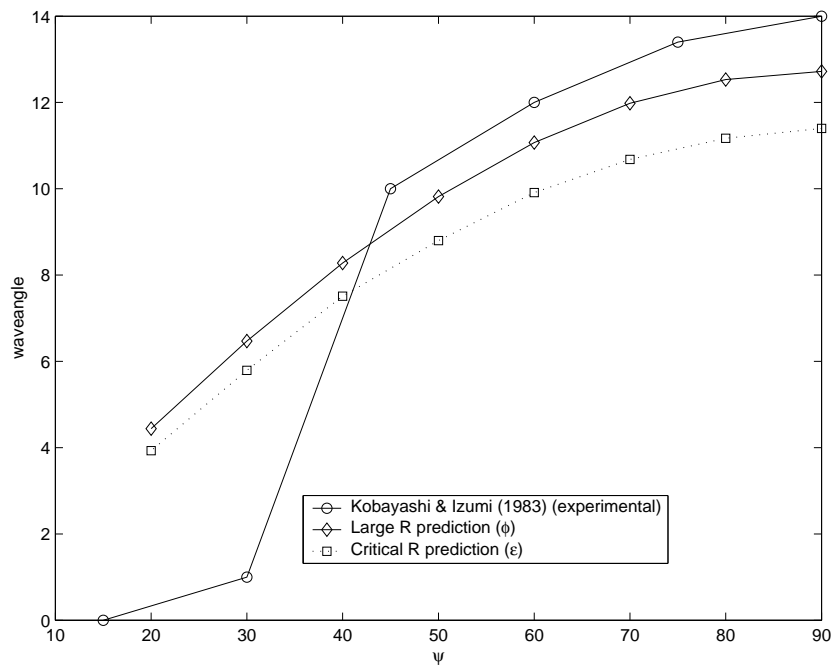


FIGURE 13. A comparison between the experimental observations of waveangle and the predicted value at the onset of type I instability and the asymptotic limit for large R.

We propose that the transition between instability mode depends on a force balance argument, which is based on the centrifugal forcing due to the basic flow in the streamwise direction and the Coriolis force in the crossflow direction. The balance of these forces determines the amount of momentum the spiral vortices carry as they are shed from the boundary layer. For slender cones, the centrifugal instability dominates and the boundary layer naturally sheds vorticity in equal and opposite directions, leading to the observed counter-rotating structures. However, as  $\psi$  is increased, the surface slope increases and the boundary layer eventually fails to possess sufficient momentum to shed vorticity in both directions; vorticity is now shed in one direction only, as the fluid is forced to roll-back due to the Coriolis force. The result is the shedding of co-rotating crossflow-dominated vortices, and the above comparisons suggest that this change takes place at around  $\psi \approx 30^\circ - 40^\circ$  where a transition from the shedding of counter-rotating to purely co-rotating vortices occurs.

The qualitative similarity of all data at large  $\psi$  in figure 13 suggests that the underlying spiral vortex structure remains unchanged. Hence, vortices are shed at similar waveangles for increasing  $\psi$  even at vastly differing Reynolds numbers.

## 6. Conclusions

In this paper we have identified the respective type I and type II modes of primary instability on the surface of a rotating cone. We have demonstrated their existence using both numerical and asymptotic analyses in the linear regime and investigated the effect of varying  $\psi$  on the important physical parameters, including the local wavenumber, local waveangle and the critical Reynolds number at onset of primary instability. Our results indicate favourable agreement with a number of previous studies, most notably with the experiments of Kobayashi & Izumi (1983). We have seen that increasing  $\psi$  leads to a rise in both type I and type II waveangles, which we attribute to the increased rotational shear effect: the spiral vortices are swept more in an azimuthal direction, due to the steep angle of the cone surface, resulting in a wider orientation angle with respect to the cone meridian. Conversely, for smaller  $\psi$ , the spiral vortices undergo a stronger forcing in the streamwise direction and hence wrap around the surface in a helical nature, propagating at a lower deviation angle from the streamwise vector. Importantly, we observe that an increase in  $\psi$  has the effect of stabilising both the type I and type II modes of crossflow instability by increasing the predicted value of the critical Reynolds number at the onset of instability. Furthermore, an increase in  $\psi$  results in the wavenumber neutral-curves undergoing a shift from left to right, which effectively expands the region of stable flow and gives rise to fewer wavenumbers in the unstable area to the right of the neutrally stable modes. Physically, in terms of aeroengine intake applications, we therefore conclude that larger values of  $\psi$  will render the flow over a central spinning nose rotor more stable, resulting in smoother airflow into the turbofan core through delaying the onset of turbulence. In addition, the consequential increase in the vortex waveangle means that airflow which is initially entrained into the boundary layer is actually shed in a direction aligned further away from the streamwise direction, both when the spiral vortices appear and when the boundary layer undergoes transition. For larger values of  $\psi$ , the desirable result is a reduction in unstable or turbulent air entering the turbofan core. It appears many modern day nose rotors are designed with this airflow shedding phenomenon in mind, and typical half-angles range from  $\psi \approx 40^\circ - 60^\circ$ .

Our study has successfully extended the comparisons between the investigations of Malik (1986) and Hall (1986) to the more general rotating cone. To this extent, for

the rigid rotating disk, we have recovered Malik's neutral-stability curves and Hall's asymptotics, together with Gajjar's type I critical layer correction (see Gajjar (2007)).

The parallel-flow approximation was made in the numerical investigation presented in §4. This approximation is found in many other boundary-layer investigations and means that the perturbation equations solved in that analysis are not rigorous at  $O(1/R)$ . Although it is acknowledged that the approximation will lead to inaccuracies at the predicted critical Reynolds numbers, it is the authors' opinion that these will be small. The excellent agreement obtained between the numerical and asymptotic investigations show that the effects of the approximation are negligible at high Reynolds number.

Throughout this investigation, we have emphasized that the crossflow instability dominates for larger half-angles, say  $\psi > 30^\circ - 40^\circ$ . Half-angles below this loose threshold region physically model a spinning missile, and in this regime an alternative mechanism appears to be the more dangerous contributor to the onset of instability. Certainly, a future investigation into these counter-rotating spirals for more slender half-angles would involve modified vortex-core length scalings, which is apparent from the visuals of Kobayashi & Izumi (1983). Such observations suggest the possibility of a viscous-mode dominated structure at work, pertaining to the onset of the centrifugal Görtler instability. A theoretical prediction of these Görtler modes, leading to a critical value of  $\psi$  where the change of instability occurs, remains an open and interesting possibility.

Importantly, our current investigation is confined to a cone rotating within still fluid. Further physical relevance to the flow over turbofan nose cones would include the introduction of an external oncoming flow, which has been studied numerically by Garrett & Peake (2007) for a range of  $\psi$ , and experimentally by Salzberg & Kezios (1965) and Kobayashi *et al.* (1983) for  $\psi = 15^\circ$ . Previous studies conclude that increasing the axial flow stabilizes the spiral vortices, hence suppressing the onset of instability. The stronger the axial flow, the stronger the stabilisation. However, work in progress suggests extending the governing parameter regime reveals the existence of a certain value of axial flow relative to the cone's rotational speed, which maximizes stability of the spiral vortex modes. We hope to report on this study in due course.

The authors wish to thank J. S. B. Gajjar and an anonymous referee for their comments. SJG wishes to acknowledge study leave granted by the University of Leicester. ZH wishes to acknowledge financial support from the School of Mathematics, University of Birmingham and the EPSRC.

#### REFERENCES

- ABRAMOWITZ, M. & STEGUN, I. A. 1964 'A Handbook of Mathematical Functions.' Dover.
- GAJJAR, J. S. B. 2007 'Nonlinear critical layers in the boundary layer on a rotating disk.' *J. Eng. Math.* **57**, 205-217.
- GARRETT, S. J. 2002 'The stability and transition of the boundary layer on rotating bodies.' PhD Thesis, Cambridge University.
- GARRETT, S. J. & PEAKE, N. 2002 'The stability and transition of the boundary layer on a rotating sphere.' *J. Fluid Mech.* **456**, 199-218.
- GARRETT, S. J. & PEAKE, N. 2004 'The stability of the boundary layer on a sphere rotating in a uniform axial flow.' *European. J. Mech. B.* **23**, 241-53.
- GARRETT, S. J. & PEAKE, N. 2007 'The absolute instability of the boundary layer on a rotating cone.' *European. J. Mech. B.* **26**, 344-53.
- GREGORY, N., STUART, J. T. & WALKER, W. S. 1955 'On the stability of three-dimensional boundary layers with application to the flow due to a rotating disk.' *Phil. Trans. R. Soc. Lond. A* **248**, 155-99.

- HALL, P. 1986 'An asymptotic investigation of the stationary modes of instability of the boundary layer on a rotating disk.' *Proc. R. Soc. Lond. A* **406**, 93-106.
- KAPPESSER, R., GREIF, R. & CORNET, I. 1973 'Mass transfer on rotating cones.' *Appl. Sci. Res.* **28**, 442-52.
- KÁRMÁN, T. VON 1921 'Über laminare und turbulente Reibung.' *Z. Angew. Math. Mech.* **1**, 233-52.
- KOBAYASHI, R., KOHAMA, Y. & KUROSAWA, M. 1983 'Boundary-layer transition on a rotating cone in axial flow.' *J. Fluid Mech.* **127**, 341-52.
- KOBAYASHI, R. & IZUMI, H. 1983 'Boundary-layer transition on a rotating cone in still fluid.' *J. Fluid Mech.* **127**, 353-64.
- KOBAYASHI, R. 1994 'Review: Laminar-to-Turbulent Transition of Three-Dimensional Boundary Layers on Rotating Bodies.' *Trans. ASME* **116**, 200-11.
- KOHAMA, Y. P. 2000 'Three-dimensional boundary layer transition study.' *Current Science* **79(6)**, 800-7.
- KREITH, F., ELLIS, D. & GIESING, J. 1962 'An experimental investigation of the flow engendered by a rotating cone.' *Appl. Sci. Res.* **A11**, 430-40.
- LINGWOOD, R. J. 1995 'Absolute instability of the boundary layer on a rotating disk.' *J. Fluid Mech.* **299**, 17-33.
- MALIK, M. R. 1986 'The neutral curve for stationary disturbances in rotating-disk flow.' *J. Fluid Mech.* **164**, 275-87.
- REED, H. L. & SARIC, W. S. 1989 'Stability of three-dimensional boundary layers.' *Ann. Rev. Fluid Mech.* **21**, 235-84.
- RESHOTKO, E. 1994 'Boundary-layer instability, transition and control.' *AIAA J.* **94**, 0001.
- SALZBERG, F. & KEZIOS, S. P. 1965 'Mass transfer from a rotating cone in axisymmetric flow.' *J. Heat Transfer* **87**, 469-76.
- SARIC, W. S., REED, H. L. & WHITE, E. B. 2003 'Stability and transition of three-dimensional boundary layers.' *Ann. Rev. Fluid Mech.* **35**, 413-40.
- SMITH, F. T. 1979 'On the non-parallel flow stability of the Blasius boundary layer.' *Proc. R. Soc. Lond. A* **366**, 91-109.
- TIEN, C. L., & CAMPBELL, D. T. 1963 'Heat and mass transfer from rotating cones.' *J. Fluid Mech.* **17**, 105-12.
- TURKYILMAZOGLU M., & GAJJAR J.S.B. 1998 'Absolute and convective instability in the incompressible boundary layer on a rotating disk.' Report no. CLSCM, University of Manchester.
- TURKYILMAZOGLU, M. 2006 'Convective and absolute instabilities in the incompressible boundary layer on a rotating disk.' *Hacettepe Journal of Mathematics and Statistics* **35**, 117-146.
- TURKYILMAZOGLU, M. 2007 'Non-linear and non-stationary modes of the lower branch of the incompressible boundary layer flow due to a rotating-disk.' *Quart. Appl. Math.* **65**, 43-68.